Nanoscale

PAPER

View Article Online
View Journal | View Issue

Cite this: *Nanoscale*, 2021, **13**, 6234

Perovskite and quantum dot tandem solar cells with interlayer modification for improved optical semitransparency and stability†

Aneta Andruszkiewicz,[a] Xiaoliang Zhang,[b] Malin B. Johansson,[a] Lin Yuan[a] and Erik M. J. Johansson *[a]

Received 24th November 2020,
Accepted 12th February 2021

DOI: 10.1039/d0nr08375e

rsc.li/nanoscale

In this work, four-terminal (4T) tandem solar cells were fabricated by using a methylammonium lead iodide ($MAPbI_3$) perovskite solar cell (PSC) as the front-cell and a lead sulfide (PbS) colloidal quantum dot solar cell (CQDSC) as the back-cell. Different modifications of the tandem interlayer, at the interface between the sub-cells, were tested in order to improve the infrared transparency of the perovskite sub-cell and consequently increase the utilization of infrared (IR) light by the tandem system. This included the incorporation of a semi-transparent thin gold electrode (Au) on the $MAPbI_3$ solar cell, followed by adding a molybdenum(VI) oxide (MoO_3) layer or a surlyn layer. These interlayer modifications resulted in an increase of the IR transmittance to the back cell and improved the optical stability, compared to that in the reference devices. This investigation shows the importance of the interlayer, connecting the PSC with a strong absorption in the visible region and the CQDSC with a strong infrared absorption to obtain efficient next-generation tandem photovoltaics (PVs).

Introduction

A multi-junction solar cell or tandem solar cell is a configuration of two or more sub-cells, which can convert sunlight into electricity with minimal energy losses. In single-junction solar cells, absorption is limited by the material's bandgap energy. Photons with energy lower than the bandgap will not be absorbed, while the photons with higher energy will generate hot carriers, which are thermalized to the band edge and in consequence lose energy in the form of heat.[1] Tandem solar cells can alleviate these energy losses. In a common tandem device, the front sub-cell with a wide bandgap material absorbs high-energy photons, while allowing lower-energy photons to pass through to be absorbed in the back sub-cell, comprised of a narrow bandgap material. The tandem cell can therefore absorb a wider spectral range and significantly reduce carrier thermalization in comparison with single-junction devices.[2] Recently, tandem solar cells with power conversion efficiency (PCE) of up to ~39% under 1 sun illumination have been reported.[3] However, they are based on the III–V semiconductors—materials with very expensive manufacturing processes.[4] Therefore, developing efficient tandem devices using low-cost materials and methods remains an important challenge.

In the last decade, tandem device structures using numerous arrangements of photoactive materials for complementary absorption have been studied. Among them, metal halide perovskite solar cells have shown tremendous potential to become a low-cost alternative for front-cells in tandem solar cells, and also for conventional photovoltaics. Metal halide perovskite solar cells in the last decade have achieved the most rapid efficiency growth of any photovoltaic material, showing a PCE increase from 3.8%[5] up to the current record value of 25.2%.[6] This remarkable performance of perovskite solar cells is possible due to their optoelectronic properties, including broad light absorption spectrum, low exciton binding energies and effective masses, long lifetime and high mobility.[7–10] Other advantages of perovskite PVs are low cost and low-temperature fabrication in comparison with the traditional silicon solar cells. Moreover, the bandgap of metal halide perovskites with the formula ABX_3 (A – monovalent cation, B – divalent cation, and X – halide anion) can be easily adjusted from 1.2 to 2.3 eV, which makes them ideal candidates for wide-bandgap absorbers in multi-junction PVs. Currently one of the best perovskite tandem photovoltaic devices can only absorb photons with a wavelength shorter than ~1000 nm (bandgap of ≳1.24 eV).[11,12] Moreover, the absorption range of the leading perovskite/Si

[a]Department of Chemistry-Ångström, Physical Chemistry, Uppsala University, 75120 Uppsala, Sweden. E-mail: erik.johansson@kemi.uu.se
[b]School of Materials Science and Engineering, Beihang University, Beijing 100191, China

†Electronic supplementary information (ESI) available. See DOI: 10.1039/d0nr08375e

tandem solar cells is limited to approximately 1100 nm (bandgap of $\gtrsim$1.12 eV).[13] It is crucial to indicate that these devices still cannot effectively harvest and convert the infrared part of the solar spectrum.

Colloidal quantum dots (CQDs) are a material of great potential in optoelectronic applications such as photovoltaics.[14–16] They offer tunable band gaps (0.5–2.0 eV), strong infrared absorption and low-cost solution processability. Given these advantages, they quickly took a firm position in the PV materials community. Lead sulfide colloidal quantum dots solar cells (PbS CQDSCs) stand out among the CQD solution-processed photovoltaics. Since they were first synthesized their efficiency has increased more than ten times, reaching over 13%.[16] This was possible due to the significant progress in surface modification and incorporation of solution-phase ligand-exchange techniques[17] in the fabrication process. Due to the CQDs' ability to reach significantly lower bandgap energy values, way beyond those of silicon and perovskites,[18] they can serve as harvesters of infrared light transmitted through wide-bandgap front-cells in multi-junction tandem photovoltaics.[19] Recent theoretical calculations by Karani *et al.* demonstrated tremendous potential for the tandem devices comprised of CQD bottom sub-cell and perovskite top cell, achieving a theoretical efficiency of 40%.[20] To date attempts to fabricate perovskite-CQD tandem devices have reported PCEs of 11% for 2-terminal (2T) and 20.2% for 4-terminal (4T) tandem configurations.[21,22]

Among the available tandem structures, 4T tandem devices seem to be more attractive due to no current-matching limitation and therefore enabling easier manufacturing processes.[23] However, constructing a successful 4T tandem solar cell entails many challenges. These involve the fabrication of an efficient, highly transparent and stable perovskite front sub-cell, the development of a spectrally matched CQD back cell with strong IR absorption and the design and modification of a semi-transparent interlayer between them. This interlayer is of crucial importance here, since it can provide semi-transparency and optical stability to the perovskite sub-cell.[22–24]

Results and discussion

In this work, a methylammonium lead iodide ($MAPbI_3$) perovskite solar cell was incorporated as the front sub-cell and a lead sulfide colloidal quantum dot solar cell was employed as the back sub-cell, as shown in Fig. 1a. Such a material combination gives spectrally matched efficient and broad absorption of both visible and near infrared light (Fig. 1b).[20] The perovskite absorbs to almost 800 nm, and the CQDs to around 1100 nm (see Fig. S1†). To improve the transmission of lower-energy photons through the cell, so that the absorption of those photons by the CQDSC can be enhanced, the interlayer is modified in this work. This includes the incorporation of a semi-transparent thin gold electrode (Au) on top of the $MAPbI_3$ solar cell, followed by the addition of a molybdenum (VI) oxide (MoO_3) or an ionomer resin interlayer. Both the thin metal electrode and metal oxide were already incorporated in our previous work to improve the transmittance of solar cell devices.[25,26] The ionomer resin used in this work was 'Surlyn' with the structure of an ethylene and methacrylic acid copolymer complexed with metal ions. It comes in the form of milky clear sheets whose transparency increases as the thickness decreases. Surlyn has high transparency, high chemical resistance, flexibility, low sealing temperature and excellent chemical compatibility with other components of solar cells. The so-called 'surlyn encapsulation' eliminates the air 'layer' between the sub-cells and consequently lowers the reflections inside the system, for improved light coupling between them. Simultaneously it improves the stability of the perovskite sub-cell. In this work, surlyn with a thickness of 25 μm was used.

Usually the perovskite solar cell is fabricated with an 80 nm thick gold top electrode. However, this counter electrode thick-

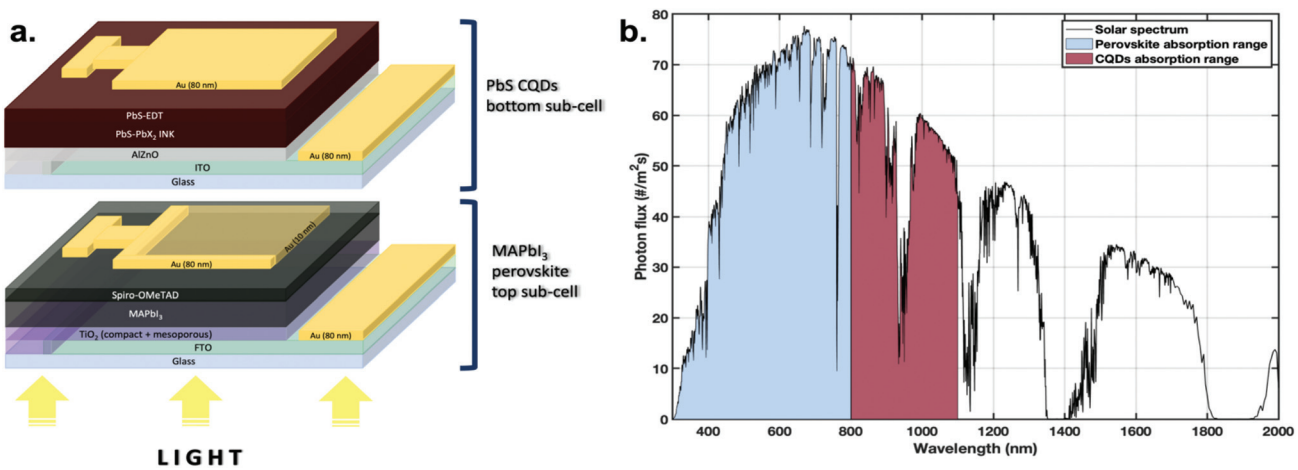

Fig. 1 Perovskite quantum dot tandem design: (a) schematic design of a 4-termianl (4T) tandem device, where the front sub-cell is $MAPbI_3$ perovskite and the back sub-cell is PbS colloidal quantum dots (PbS CQDs). (b) Solar spectrum with highlighted light absorption regions for both perovskite and CQD solar cells in this work.

ness significantly reduces the device's transmittance. Therefore, we compared different thicknesses of the Au electrode on top of the perovskite cell, namely 10, 15 and 80 nm. The highest transmittance in the IR region was observed for the 10 nm Au layer (Fig. 2a). We incorporated here a patterned design of the Au electrode on the perovskite sub-cell, as shown in Fig. 1a and Fig. S2† to improve the charge collection and therefore increase the short-circuit current (J_{sc}), the fill factor (FF) and subsequently the PCE of the perovskite cell, without losing the cell semi-transparency.

As mentioned above, the incorporation of metal oxide on top of the Au in the solar cell should lead to improved device transmittance. Here we tested 3 different thicknesses of MoO_3, namely 20, 30 and 40 nm, on a 10 nm thick semi-transparent gold electrode. The transparency improvement was recorded for the 40 nm molybdenum(VI) oxide layer, resulting in ~40% transmittance in the near-infrared region (see Fig. S3†). However, the devices fabricated with this interlayer modification suffered from significant losses in the current–voltage performance (see Fig. S4†). This was most probably influenced by interactions of MoO_3 with the Spiro-OMeTAD layer.

In the next step, CQD-perovskite 4T tandem devices were fabricated by stacking the semi-transparent $MAPbI_3$ perovskite solar cell with a 10 nm Au electrode on top of the PbS CQD solar cell. Measurements of the current–voltage (J–V) characteristics and power conversion efficiency (PCE) were carried out following previously reported methods.[27,28] The J–V characteristics of the best semi-transparent perovskite cell and PbS CQD solar cells, are shown in Fig. 3a. A Surlyn interlayer was applied in the tandem devices with the perovskite front-cell and PbS CQD back-cell. When the perovskite cell was applied on top of the CQDSC, a decrease in the PCE of the CQDSC was observed, as expected from the reduced light intensity reaching the bottom CQDSC in the tandem configuration. The incident photon-to-current conversion efficiency (IPCE) in Fig. 3b shows that the perovskite solar cell converts light up to almost 800 nm, and that the CQDSC converts light up to around 1100 nm. Finally, the efficiency of the 4T tandem structure by combining the semi-transparent $MAPbI_3$ front-cell and the PbS CQD back-cell using a surlyn interlayer was 18.9% (see Table 1). Therefore, a clear performance enhancement in the tandem cells compared to each single sub-cell was achieved due to better light utilization and reduced carrier thermalization. The statistics of the solar cell parameters for several cells are shown in Fig. S5.†

To analyze the effect of the surlyn interlayer, the photovoltaic average parameters for tandem devices before and after inclusion of the surlyn interlayer were compared and the results are shown in Fig. 4. The same devices were compared with and without surlyn, to see the actual improvement of the surlyn incorporation for each device.

On the average, ~13% increase in the PCE and ~8% increase in J_{sc} were observed for filtered PbS CQDs solar cell samples after adding surlyn into the interlayer design (Fig. 4a). This shows that the surlyn interlayer improves the light transmission to the CQD bottom-cell, by the reduction of reflections at the interfaces. The 'surlyn encapsulation' approach also improved the optical stability of semi-transparent $MAPbI_3$ devices. The non-encapsulated devices showed approximately 10% higher transmittance in the visible region in comparison with the encapsulated samples, over a period of 7 days under the AM 1.5 illumination in air, as seen in Fig. 4b. This shows that the degradation of the $MAPbI_3$ perovskite layer in the encapsulated samples is also reduced.

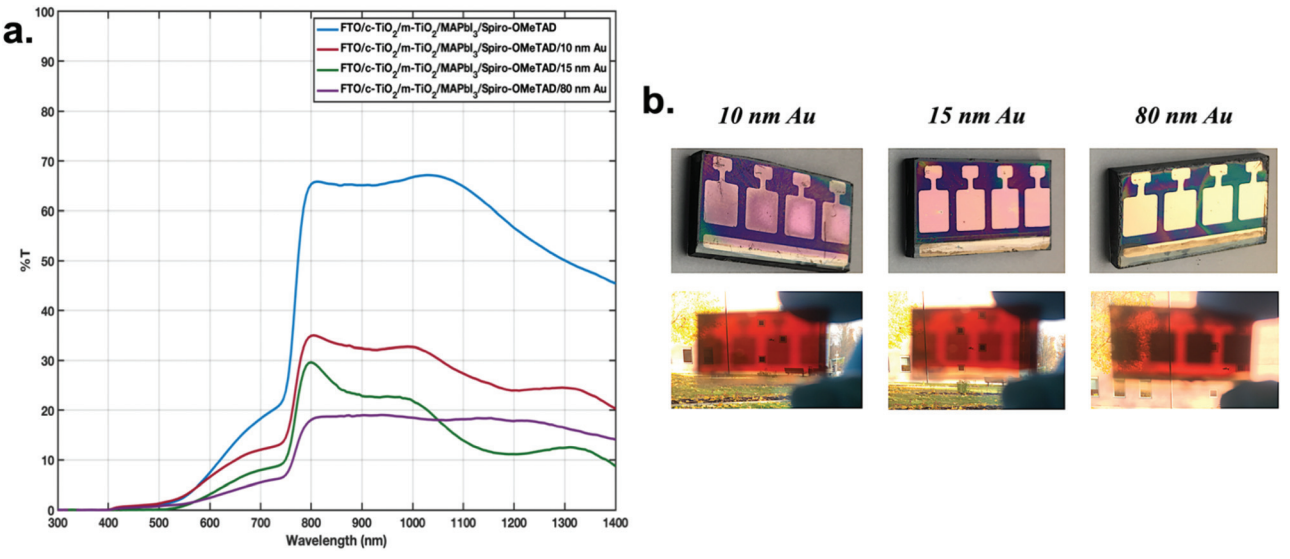

Fig. 2 Optimized IR transparency of the front-cell: (a) transmittance spectrum of the perovskite solar cell with the following structure: FTO glass/compact TiO_2/mesoporous TiO_2/$MAPbI_3$ perovskite/Spiro-OMeTAD with different thicknesses of the Au electrode. (b) Pictures of the semi-transparent $MAPbI_3$ solar cells of 2.4 × 1.4 cm size with different thicknesses of the Au electrode: top and cross views.

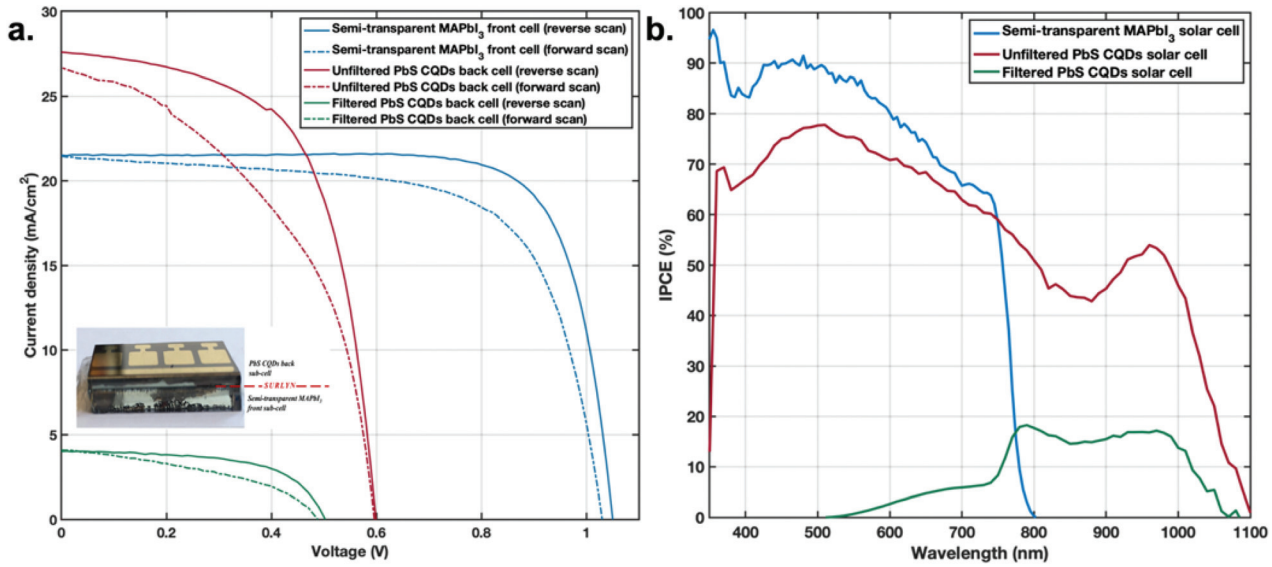

Fig. 3 Photovoltaic performance: (a) current–voltage (J–V) characteristics of unfiltered (red line) and filtered (green line) PbS CQD devices and the semi-transparent $MAPbI_3$ device (blue line), under illumination (1000 W m^{-2}, AM 1.5G). The semi-transparent $MAPbI_3$ solar cell structure is as follows: FTO glass/compact TiO_2/mesoporous TiO_2/$MAPbI_3$ perovskite/Spiro-OMeTAD/10 nm Au/surlyn (25 μm). The PbS CQD solar cell has the following configuration: indium doped tin oxide (ITO) glass/aluminum doped zinc oxide layer (AlZnO)/PbS-PbX_2 (X-halogen molecule)/PbS-EDT (EDT-1,2-ethanedithiol)/80 nm Au. PbS CQDs of λ_{max} = 935 nm were used for these measurements. The filtered PbS CQD cell means that during the measurement, the semi-transparent $MAPbI_3$ solar cell was placed above the CQD cell – see the included profile picture of the perovskite-CQD tandem solar cell (2.4 × 1.4 cm in size). (b) IPCE spectra of the PbS CQD cell (red line), the $MAPbI_3$ perovskite cell with a 10 nm semi-transparent Au electrode (blue line) and the filtered PbS CQD cell with a semi-transparent $MAPbI_3$ cell as the filter (green line).

Table 1 Summary of the photovoltaic performance of the champion 4T perovskite-CQD tandem solar cell, together with the performance of individual components

Device	V_{oc} (V)	J_{sc} (mA cm^{-2})	Fill factor (%)	PCE (%)
Semi-transparent $MAPbI_3$ front cell (reverse scan)	1.050	−21.50	76.9	17.37
Semi-transparent $MAPbI_3$ front cell (forward scan)	1.030	−21.45	67.3	14.88
Unfiltered PbS CQDs back cell (reverse scan)	0.598	−27.58	61.0	10.06
Unfiltered PbS CQDs back cell (forward scan)	0.595	−26.67	46.6	7.40
Filtered PbS CQDs back cell (reverse scan)	0.517	−4.83	61.1	1.53
Filtered PbS CQDs back cell (forward scan)	0.500	−4.82	43.4	1.05
4-Terminal tandem solar cell (reverse scan)	—	—	—	18.90
4-Terminal tandem solar cell (forward scan)	—	—	—	15.93

Experimental

PbS CQD synthesis

PbS CQDs were synthesized following a previously published method.[29] First, 933 mg of lead(II) oxide (PbO, 99.999%, Sigma-Aldrich), 20 g of octadecane (ODE, technical grade, 90%, Sigma-Aldrich) and 4.056 g of oleic acid (OA, technical grade, 90%, Sigma-Aldrich) were mixed together. The solution was degassed under vacuum and then heated to 100 °C for 2 h under a nitrogen atmosphere. For the sulfur precursor, 356 mg of hexamethyldisilathiane (HMDST, synthesis grade, Sigma-Aldrich) was dissolved in 10 mL of octadecane and degassed under vacuum, heated at 80 °C for 2 h and then loaded into a syringe. Next, the temperature of the PbO, ODE and OA solution was reduced to 90 °C and the HMDST solution was rapidly injected. Directly after the injection, the solution was removed from the heat and allowed to cool down to room temperature. Such synthesized CQDs were purified by precipitation with acetone, followed by centrifugation at 5000 rpm for 5 min and redispersion in toluene (anhydrous, 99.8%, Sigma-Aldrich). This washing was repeated twice and the final precipitate was dispersed in 10 mL of octane (reagent grade, 90%, Sigma-Aldrich).

AlZnO (AZO) sol–gel synthesis

2.195 g of zinc acetate dihydrate (99.5%, Merck) and 198 mg of aluminum(III) nitrate nonahydrate (>98.5%, Sigma-Aldrich) were mixed with 20 mL of ethanol. The solution was heated to 80 °C and stirred for 5 min. Then 0.65 mL of ethanolamine (99.5%, Sigma-Aldrich) was injected. Such a solution was left

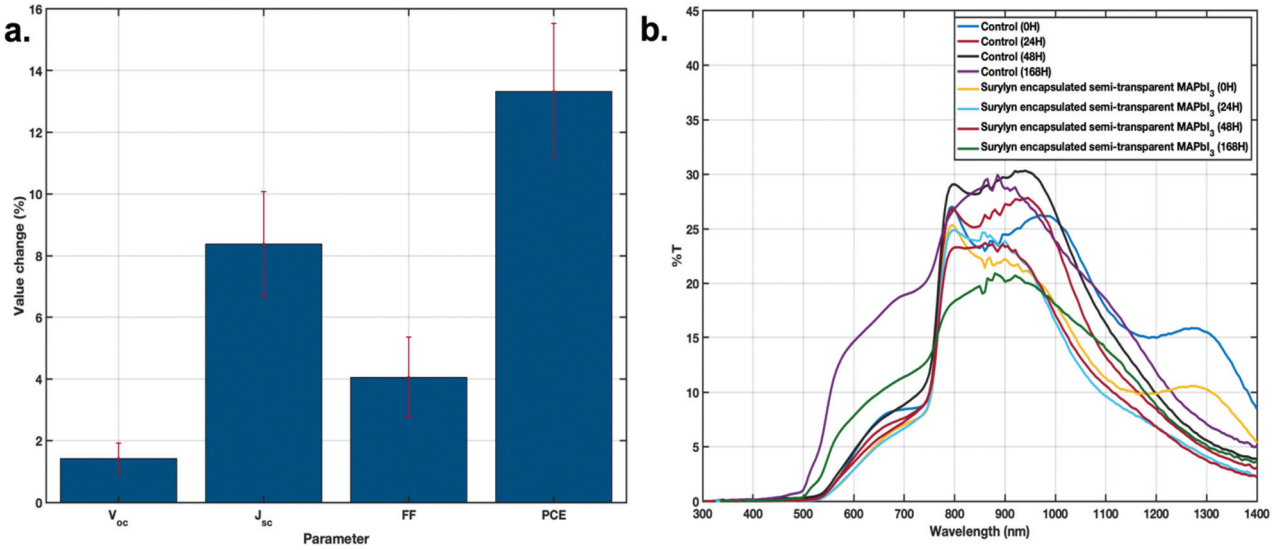

Fig. 4 (a) Percentage value of an average increase in photovoltaic parameters after incorporating surlyn into the tandem solar cell structure. For this statistical measurement, 12 samples of PbS CQD solar cells with λ_{max} values equal to both 901 and 935 nm, respectively, were used. (b) Optical stability measurements for tandem solar cells after incorporation of surlyn into the device structure. The control sample is the non-encapsulated semi-transparent $MAPbI_3$ solar cell with the following structure: FTO/c-TiO_2/m-TiO_2/$MAPbI_3$ perovskite/Spiro-OMeTAD/10 nm Au. Surlyn-encapsulated $MAPbI_3$ samples have the following composition: FTO/c-TiO_2/m-TiO_2/$MAPbI_3$ perovskite/Spiro-OMeTAD/10 nm Au/surlyn/ITO/AlZnO.

under stirring for 3 h. After that, heating was stopped and the reaction mixture was allowed to cool down to room temperature.

AZO film deposition

Pre-etched indium-doped tin oxide (ITO) glass (ITO coated glass for R&D use from Kaivo) was cleaned with detergent, acetone and ethanol. Then 20 min of UV-ozone treatment was performed. AZO sol–gel was filtered through a syringe filter (0.45 μm) and 150 μm of film was spin-coated on each pre-treated glass sample of 2.4 × 2.8 cm size at 3000 rpm for 30 s. Then, two-step annealing of the deposited film was performed under the following conditions: 200 °C for 30 min, followed by 300 °C for 30 min.

CQD solar cells fabrication

A solution ligand exchange process was performed according to a previously published paper.[17] 7.5 mL of a 10 mg mL^{-1} solution of PbS CQDs in octane was vortexed for 5 min with 12 mL of *N*,*N*-dimethylformamide (anhydrous, 99.8%, Sigma-Aldrich) solution containing 0.1 M lead(II) iodide (PbI_2, 99.99%, TCI), 0.04 M lead(II) bromide ($PbBr_2$, >98.0%, TCI) and 0.06 M ammonium acetate (AA, for molecular biology, ≥98%, Sigma-Aldrich). The reaction was subsequently washed with octane 3 times. Then, 12 mL of toluene was added. Precipitated particles were centrifuged at 4000 rpm for 5 min and re-dispersed in butylamine, with a final concentration of 300 mg mL^{-1}. 45 μL of such prepared INK was spin-coated on the AZO/ITO glass samples of 2.8 × 2.4 cm size, using a two-step process: 1000 rpm for 3 s, followed by 1800 rpm for 30 s. The samples were annealed at 70 °C for 10 min. PbS-EDT layers were deposited by spin coating in the following manner. First 50 μL of a 50 mg mL^{-1} PbS CQD solution in octane was spin-coated at 1800 rpm for 30 s. Next, ligand exchange was performed by deposition of 200 μL of 0.01% (V/V) 1,2-ethanedithiol (EDT, ≥98%, Sigma-Aldrich) in acetonitrile (ACN, anhydrous, 99.8%, Sigma-Aldrich) solution for 30 seconds and followed by spin-coating of this solution in 1800 rpm for 30 s. Finally, double acetonitrile rinsing was executed by two following spin-coatings of 200 μL of ACN at 1800 rpm for 30 s each. Then the samples were cut in half to obtain cells of 1.4 × 2.4 cm size. As a final step, 80 nm of gold contact was evaporated, using a thermal-deposition method.

$MAPbI_3$ solar cell fabrication

Perovskite solar cells were fabricated using TEC15 fluorine-doped tin oxide (FTO) glass from Pilkington. FTO glass was chemically etched using Zn powder and a 2 M hydrochloric acid solution. Multiple glass cleaning steps were carried out: RBS/water solution, acetone, ethanol and UV-Ozone treatment. Next, the electron transport layer was deposited. First, a compact titanium dioxide layer (c-TiO_2) was prepared by high-temperature spray pyrolysis of a titanium diisopropoxide bis (acetylacetonate) (75 wt% in isopropanol, Sigma-Aldrich) solution in ethanol (1 : 9 volume ratio). This layer was deposited at 500 °C and annealed for 30 min at the same temperature. After cooling down the samples to room temperature, they were cut into rectangles of 1.4 × 2.4 cm size and a mesoporous TiO_2 layer (m-TiO_2) was deposited as follows: 1.5 g of TiO_2 paste (30 NR-D, GreatCell Solar) was dispersed in 10 mL of ethanol and spin-coated on the c-TiO_2 layer at 4000 rpm for 20 s. Then, such prepared samples were annealed at 450 °C for

30 min. The $MAPbI_3$ perovskite absorber layer was deposited inside a N_2 glovebox. The precursor of the perovskite films was prepared by dissolving 415 mg of PbI_2 and 143 mg of methylammonium iodide (MAI, 99.99%, Dyenamo) in DMF : DMSO (4 : 1 volume ratio) solvent mixture. The perovskite layer was spin-coated onto the m-TiO_2 at 4000 rpm for 30 s. After 15 s of spin-coating, chlorobenzene (CB, anhydrous, 99.8%, Sigma-Aldrich) was added dropwise onto the substrate. Such fabricated substrates were annealed at 90 °C for 30 min. The hole transporting layer (HTL), in the form of spiro-OMeTAD (min. 99.8%, Borun New Material technology Ltd), was deposited right after the fabrication of perovskite films. The spiro-OMeTAD solution was prepared beforehand by dissolving 52 mg of spiro-OMeTAD in 568.8 μL of chlorobenzene. Next, 20.5 μL of 4-tertbutyl-pyridine was added, followed by 11.8 μL of a lithium bis(trifluoromethanesulfonyl)imide solution in acetonitrile (516 mg mL^{-1}) and 5.09 μL of a tris(2-(1*H*-pyrazol-1-yl)-4-*tert*-butylpyridine)cobalt(III) tri[bis(trifluoromethane)sulfonimide] (FK 209 Co(III)-TFSI salt) solution in acetonitrile (37.5 mg mL^{-1}). This solution was spin-coated on top of the perovskite films at 2500 rpm for 30 s. After that, the samples were kept in the dark and under an ambient atmosphere for oxidation.

Interlayer modifications

All prepared devices were of 1.4 × 2.4 cm size. For the opaque devices, 80 nm of gold was evaporated on top of spiro-OMeTAD by thermal-deposition in a vacuum. For the semi-transparent devices, three different modifications were applied. The first type of device was fabricated with a thin Au back electrode, prepared by the deposition of a 10 nm Au layer, followed by an additional 70 nm Au frame on the edges of the 10 nm Au contact (see Fig. 1a) for better charge collection. For the second type of semi-transparent device, the aforementioned thin Au back electrode was topped with a molybdenum(VI) oxide (MoO_3, 99.97%, Sigma-Aldrich) layer for better transmittance. The third type of semi-transparent device was fabricated by deposition of the aforementioned thin Au back electrode topped with a 25 μm surlyn piece to minimize reflections. Gold and MoO_3 were deposited using thermal evaporation. Surlyn was deposited by placing the perovskite cell on the hotplate, placing a piece of surlyn on top of the cell and heating the hotplate to 70 °C. Then, the CQD SC (glass side) was placed on top of the surlyn and both cells were manually pressed together.

Solar cell performance measurements and characterization

IPCE spectra were recorded with a computer-controlled system comprised of a xenon lamp (Spectra products ASBXE 175), a monochromator (Spectra Products CM110), a LabJack U6 and a potentiostat (PINE AFRDE 5). Measurements were executed after a previously performed calibration with a certified reference solar cell (Fraunhofer ISE). Transmission measurements were performed with a PerkinElmer Lambda 900 spectrometer. Photovoltaic performance was measured by illuminating the samples with AM1.5G sunlight provided by a self-calibrating WaveLabs SINUS-70 solar simulator with UV and IR range extenders while measuring the cell's current–voltage response with an Ossila X200 source meter. Black masking was applied on top of the cell with an aperture of 0.065 cm^2 for filtered and unfiltered PbS CQD back sub-cells and of 0.125 cm^2 for semi-transparent $MAPbI_3$ solar cells.

Conclusions

In conclusion, tandem solar cells based on a methylammonium lead iodide ($MAPbI_3$) perovskite solar cell (PSC) as the front-cell and a lead sulfide (PbS) colloidal quantum dot (CQD) solar cell as the back-cell, with different interlayer modifications, have been investigated. The $MAPbI_3$ perovskite top cell, with a thin semi-transparent 10 nm gold electrode, yielded a PCE of ~17.3% and increased transmittance of IR light in comparison with the standard 80 nm Au electrode. Further development with an additional MoO_3 layer was also performed, leading to enhanced transmittance of IR light, but with lower photovoltaic performance compared to the case without the MoO_3 layer. Therefore, incorporation of surlyn encapsulation on top of the thin Au electrode was instead investigated, showing the enhanced optical transmittance of infrared light to the PbS CQD back cell. The surlyn interlayer also leads to the increased optical stability of the perovskite solar cell. The *J–V* performance of the four-terminal tandem solar cell with $MAPbI_3$ perovskite as the front cell and PbS CQDs as the back sub-cell and a surlyn interlayer was demonstrated, with an efficiency of 18.9%. The surlyn interlayer resulted in around 13% enhanced PCE compared to a tandem cell without the surlyn interlayer. These results show that modifications of the interlayer in perovskite-CQD 4T tandem devices can lead to better utilization of the infrared part of the light spectrum and higher stability. Furthermore, incorporation of different perovskite structures or adjustment in the size of the quantum dots in the CQD solar cell could also significantly improve the tandem performance. Consequently, such tandem devices with an optimized interlayer may be a very interesting and promising alternative for next-generation photovoltaics.

Conflicts of interest

There are no conflicts to declare.

Acknowledgements

The authors acknowledge the financial support obtained from the Swedish Energy Agency, Olle Engkvist Foundation and ÅForsk. This work was also supported by the National Science Foundation of China (51872014), the Recruitment Program of Global Experts, the Fundamental Research Funds for the Central Universities (YWF-20-BJ-J-637) and the "111" project (B17002).

References

1 A. Polman, M. Knight, E. C. Garnett, B. Ehrler and W. C. Sinke, *Science*, 2016, **352**, aad4424.
2 Q. Wali, N. K. Elumalai, Y. Iqbal, A. Uddin and R. Jose, *Renewable Sustainable Energy Rev.*, 2018, **84**, 89–110.
3 M. A. Green, Y. Hishikawa, W. Warta, E. D. Dunlop, D. H. Levi, J. Hohl-Ebinger and A. W. H. Ho-Baillie, *Prog. Photovoltaics Res. Appl.*, 2017, **25**, 668–676.
4 R. Cariou, J. Benick, P. Beutel, N. Razek, C. Flotgen, M. Hermle, D. Lackner, S. W. Glunz, A. W. Bett, M. Wimplinger and F. Dimroth, *IEEE J. Photovoltaics*, 2017, **7**, 367–373.
5 A. Kojima, K. Teshima, Y. Shirai and T. Miyasaka, *J. Am. Chem. Soc.*, 2009, **131**, 6050–6051.
6 https://www.nrel.gov/pv/assets/pdfs/best-research-cell-efficiencies.20190802.pdf.
7 S. De Wolf, J. Holovsky, S. J. Moon, P. Löper, B. Niesen, M. Ledinsky, F. J. Haug, J. H. Yum and C. Ballif, *J. Phys. Chem. Lett.*, 2014, **5**, 1035–1039.
8 K. Galkowski, A. Mitioglu, A. Miyata, P. Plochocka, O. Portugall, G. E. Eperon, J. T. W. Wang, T. Stergiopoulos, S. D. Stranks, H. J. Snaith and R. J. Nicholas, *Energy Environ. Sci.*, 2016, **9**, 962–970.
9 D. P. McMeekin, G. Sadoughi, W. Rehman, G. E. Eperon, M. Saliba, M. T. Hörantner, A. Haghighirad, N. Sakai, L. Korte, B. Rech, M. B. Johnston, L. M. Herz and H. J. Snaith, *Science*, 2016, **351**, 151–155.
10 L. M. Herz, *ACS Energy Lett.*, 2017, **2**, 1539–1548.
11 G. E. Eperon, M. T. Hörantner and H. J. Snaith, *Nat. Rev. Chem.*, 2017, 0095.
12 G. E. Eperon, T. Leijtens, K. A. Bush, R. Prasanna, T. Green, J. T. W. Wang, D. P. McMeekin, G. Volonakis, R. L. Milot and R. May, *Science*, 2016, 861–865.
13 M. H. Futscher and B. Ehrler, *ACS Energy Lett.*, 2017, 2089–2095.
14 L. Hu, Z. Zhang, R. J. Patterson, Y. Hu, W. Chen, C. Chen, D. Li, C. Hu, C. Ge, Z. Chen, L. Yuan, C. Yan, N. Song, Z. L. Teh, G. J. Conibeer, J. Tang and S. Huang, *Nano Energy*, 2018, **46**, 212–219.
15 X. Zhang, D. Jia, C. Hägglund, V. A. Öberg, J. Du, J. Liu and E. M. J. Johansson, *Nano Energy*, 2018, **53**, 373–382.
16 M. J. Choi, F. P. García de Arquer, A. H. Proppe, A. Seifitokaldani, J. Choi, J. Kim, S. W. Baek, M. Liu, B. Sun, M. Biondi, B. Scheffel, G. Walters, D. H. Nam, J. W. Jo, O. Ouellette, O. Voznyy, S. Hoogland, S. O. Kelley, Y. S. Jung and E. H. Sargent, *Nat. Commun.*, 2020, **11**, 1–9.
17 M. Liu, O. Voznyy, R. Sabatini, F. Pelayo García De Arquer, R. Munir, A. Hesham Balawi, X. Lan, F. Fan, G. Walters, A. R. Kirmani, S. Hoogland, F. Laquai, A. Amassian and E. H. Sargent, *Nat. Mater.*, 2017, **16**, 258–263.
18 E. H. Sargent, *Nat. Photonics*, 2012, **6**, 133–135.
19 A. H. Ip, A. Kiani, I. J. Kramer, O. Voznyy, H. F. Movahed, L. Levina, M. M. Adachi, S. Hoogland and E. H. Sargent, *ACS Nano*, 2015, **9**, 8833–8842.
20 A. Karani, L. Yang, S. Bai, M. H. Futscher, H. J. Snaith, B. Ehrler, N. C. Greenham and D. Di, DOI: 10.1021/acsenergylett.8b00207.
21 Y. Zhang, M. Gu, N. Li, Y. Xu, X. Ling, Y. Wang, S. Zhou, F. Li, F. Yang, K. Ji, J. Yuan and W. Ma, *J. Mater. Chem. A*, 2018, **6**, 24693–24701.
22 A. Manekkathodi, B. Chen, J. Kim, S. W. Baek, B. Scheffel, Y. Hou, O. Ouellette, M. I. Saidaminov, O. Voznyy, V. E. Madhavan, A. Belaidi, S. Ashhab and E. Sargent, *J. Mater. Chem. A*, 2019, **7**, 26020–26028.
23 T. Leijtens, K. A. Bush, R. Prasanna and M. D. McGehee, *Nat. Energy*, 2018, **3**, 828–838.
24 C. Li, Y. Wang and W. C. H. Choy, *Small Methods*, 2020, **4**, 1–19.
25 X. Zhang, C. Hägglund, M. B. Johansson, K. Sveinbjörnsson and E. M. J. Johansson, *Adv. Funct. Mater.*, 2016, **26**, 1921–1929.
26 X. Zhang, C. Hä and E. M. J. Johansson, *Energy Environ. Sci.*, 2017, **10**, 216.
27 D. Zhao, Y. Yu, C. Wang, W. Liao, N. Shrestha, C. R. Grice, A. J. Cimaroli, L. Guan, R. J. Ellingson, K. Zhu, X. Zhao, R. G. Xiong and Y. Yan, *Nat. Energy*, 2017, **2**, 1–7.
28 J. Tong, Z. Song, D. H. Kim, X. Chen, C. Chen, A. F. Palmstrom, P. F. Ndione, M. O. Reese, S. P. Dunfield, O. G. Reid, J. Liu, F. Zhang, S. P. Harvey, Z. Li, S. T. Christensen, G. Teeter, D. Zhao, M. M. Al-Jassim, M. F. A. M. Van Hest, M. C. Beard, S. E. Shaheen, J. J. Berry, Y. Yan and K. Zhu, *Science*, 2019, **364**, 475–479.
29 G. H. Kim, B. Walker, H. B. Kim, E. H. Sargent, J. Park and J. Y. Kim, *Adv. Mater.*, 2014, **26**, 3321–3327.